

Solution of Physics-based Bayesian Inverse Problems with Deep Generative Priors

Dhruv V Patel, Deep Ray and Assad A Oberai¹

¹Department of Aerospace and Mechanical Engineering, University of Southern California, Los Angeles, California, USA

Abstract

Inverse problems are notoriously difficult to solve because they can have no solutions, multiple solutions, or have solutions that vary significantly in response to small perturbations in measurements. Bayesian inference, which poses an inverse problem as a stochastic inference problem, addresses these difficulties and provides quantitative estimates of the inferred field and the associated uncertainty. However, it is difficult to employ when inferring vectors of large dimensions, and/or when prior information is available through previously acquired samples. In this paper, we describe how deep generative adversarial networks can be used to represent the prior distribution in Bayesian inference and overcome these challenges. We apply these ideas to inverse problems that are diverse in terms of the governing physical principles, sources of prior knowledge, type of measurement, and the extent of available information about measurement noise. In each case we apply the proposed approach to infer the most likely solution and quantitative estimates of uncertainty.

1 Introduction

The definition of what constitutes an inverse problem is not very precise. In his article titled *Inverse Problems*, Joseph Keller [1] defines two problems as inverses of each other if the formulation of one involves the complete or partial solution of the other. Under these conditions the problem that has been studied extensively is termed as the “direct problem”, and the one that is newer, and not as well studied, is called the “inverse problem.” The author then gives some serious and some not-so-serious examples of inverse problems. For the purpose of this paper, a typical direct problem is one of finding the temperature field in a Fourier solid with a prescribed heat source, boundary conditions, and thermal conductivity. The corresponding inverse problem is that of finding the thermal conductivity field given the temperature field. Similar inverse problems are at the core of techniques that infer mechanical properties of tissue [2, 3], X-ray tomography, inverse acoustic/electromagnetic scattering [4, 5], geophysics [6, 7], climate modeling [8, 9], and astronomy [10, 11].

In addition to being newer and less well-studied, most inverse problems are ill-posed in the sense of Hadamard [12]. That is, they either have multiple solutions (non-unique), no solutions (non-existence), or have solutions that vary significantly in response to small perturbations in measured data (unstable). Further, they are driven by measured input that is almost always corrupted with stochastic noise. One approach to address these challenges relies on “regularizing” the inverse problem which amounts to solving an alternate well-posed problem whose solution is close to the original inverse problem. Another approach, which is often referred to as Bayesian inference, involves viewing the inverse problem as a stochastic inference problem and using

Bayes’ rule to update the prior probability distribution of the solution with the knowledge gained from the measurement [13, 14]. A significant advantage of Bayesian inference is that it provides quantitative estimates of the probability distribution of the solution which can be used to quantify the confidence in the solution.

The application of Bayesian inference to practical problems leads to two significant challenges. The first involves selecting a prior probability distribution that encodes all the available knowledge about the solution. Most practitioners use simple distributions as the prior distribution, like the multivariate Gaussian distribution or Gaussian processes with specified covariance kernels or hierarchical priors. However, the true prior distribution may be much more complex (see Figure 2 for example). The second challenge is the so-called *curse of dimensionality*, which occurs when the dimension of the solution vector is large. In this case sampling from the posterior distribution using methods like Markov Chain Monte Carlo (MCMC) becomes prohibitively expensive.

In this paper we consider problems in which prior knowledge about the solution is available in the form of many independent and identically distributed samples drawn from the true prior distribution. We describe how a generative adversarial network (GAN) [15], a type of a deep neural network, may be used to encode this information and perform Bayesian inference. This is accomplished by mapping a simple distribution in the low-dimensional latent space of the GAN to the complex prior distribution in the space of the solution vector. Further, we map the expression of the posterior distribution into the latent space of the GAN and utilize the fact that its dimension is typically much smaller than that of the solution space to achieve dimension reduction. We demonstrate the broad applicability of these ideas by solving inverse problems with different direct problems (heat equation, Navier’s equations for elasticity and the Radon transform), different prior distributions (simple geometrical features, MNIST digits, material micro-structure and the Shepp-Logan phantom) and synthetic and experimentally measured data. When possible, we compare our results with “true” values, other commonly used inference methods, and experimental measurements.

We recognize that several other researchers have utilized GANs in different aspects of Bayesian inference. In [16], GANs are used to directly learn the posterior distribution of the solution. This is accomplished by constructing a generator whose output is conditioned on the measurement vector. In [17], also a conditional version of a GAN is used; however the output of the generator is conditioned on the spatial coordinates for the problem, and the direct problem is also solved within the network by appending to the loss function a term that penalizes the residual of direct problem. In contrast to these methods, we explore the use of GANs in approximating the prior in Bayesian inference. This is an extension of our recent work [18] to problems where the direct map, which is derived from the underlying physics, is known. We also note that the field of sample based priors [19, 20] and the idea of reducing the dimension of parameter space [21, 22, 23] have a rich history of methods that do not rely on using GANs.

2 Results

2.1 Bayesian inference

Consider the following direct model

$$\mathbf{f} : \mathbf{x} \mapsto \mathbf{y}, \quad \mathbf{x} \in \Omega_{\mathcal{X}} \subset \mathbb{R}^{N_{\mathcal{X}}}, \quad \mathbf{y} \in \Omega_{\mathcal{Y}} \subset \mathbb{R}^{N_{\mathcal{Y}}}, \quad (1)$$

where \mathbf{y} is the measured response for some input \mathbf{x} . Direct problems are generally well studied and have robust numerical solvers. On the other hand, inverse problems, where we wish to infer \mathbf{x} given a measurement \mathbf{y} , are challenging. Bayesian inference provides a way of solving inverse problems with quantified uncertainty estimates. Within this approach the inferred field and

observations are modeled using the random variables \mathcal{X} and \mathcal{Y} , respectively. It is often assumed that the measurement is corrupted by an additive noise, i.e., $\hat{\mathbf{y}} = \mathbf{y} + \boldsymbol{\eta}$, where $\boldsymbol{\eta}$ is the noise and p_η is its distribution. A prior distribution $p_{\mathcal{X}}^{\text{prior}}(\mathbf{x})$, which encodes the knowledge about \mathcal{X} prior to observing $\hat{\mathbf{y}}$, is assumed. This is used along with the likelihood of observing the measurement $\hat{\mathbf{y}}$, given $\mathcal{X} = \mathbf{x}$, that is $p_{\mathcal{Y}}^{\text{like}}(\hat{\mathbf{y}}|\mathbf{x})$. Using Bayes' rule, this yields the following expression for the posterior distribution of \mathcal{X} ,

$$p_{\mathcal{X}}^{\text{post}}(\mathbf{x}|\hat{\mathbf{y}}) = \frac{p_{\mathcal{Y}}^{\text{like}}(\hat{\mathbf{y}}|\mathbf{x})p_{\mathcal{X}}^{\text{prior}}(\mathbf{x})}{p_{\mathcal{Y}}(\hat{\mathbf{y}})} \propto p_\eta(\hat{\mathbf{y}} - \mathbf{f}(\mathbf{x}))p_{\mathcal{X}}^{\text{prior}}(\mathbf{x}), \quad (2)$$

where $p_{\mathcal{Y}}(\hat{\mathbf{y}})$ is called the evidence. The likelihood term, $p_{\mathcal{Y}}^{\text{like}}(\hat{\mathbf{y}}|\mathbf{x}) = p_\eta(\hat{\mathbf{y}} - \mathbf{f}(\mathbf{x}))$, injects physics into the framework via the direct operator \mathbf{f} . Statistical inference involves characterizing the posterior distribution by computing a statistical quantity of interest (QoI) (defined by $l(\mathbf{x})$) with respect to this posterior,

$$\mathbb{E}_{\mathbf{x} \sim p_{\mathcal{X}}^{\text{post}}(\mathbf{x}|\hat{\mathbf{y}})} [l(\mathbf{x})] = \int_{\Omega_{\mathcal{X}}} l(\mathbf{x})p_{\mathcal{X}}^{\text{post}}(\mathbf{x}|\hat{\mathbf{y}})d\mathbf{x}. \quad (3)$$

For most problems of practical interest, the dimension of the inferred field is typically large ($\mathcal{O}(10^2 - 10^6)$), and the integral (3) cannot be computed using a standard numerical/quadrature-based method; instead it is approximated using MCMC methods [24].

There are two major challenges in using the Bayesian framework described above. First, constructing a closed-form expression of the prior, $p_{\mathcal{X}}^{\text{prior}}(\mathbf{x})$, is challenging, especially when the prior information is available through samples. Consider, for example, samples of the microstructure of a material shown in Figure 2(c) or the Shepp-Logan phantom of the human head shown in Figure 2(g). It should be clear that the variability in this data cannot be modeled using standard distributions, or their mixtures. Second, for problems with high dimensional parameter space, the number of MCMC samples required for a well-mixed Markov chain is large, making it difficult to accurately approximate the QoI. In the development below, we describe how a GAN, a type of a deep learning algorithm, can be used to address these challenges.

2.2 Bayesian inference with GAN priors

GANs typically comprise two neural networks that are trained adversarially to learn a target distribution $p_{\mathcal{X}}(\mathbf{x})$ and generate samples from it. The generator \mathbf{g} maps a latent variable $\mathbf{z} \in \Omega_{\mathcal{Z}}$ sampled from $p_{\mathcal{Z}}$ to the space of the target field \mathbf{x} , and the discriminator is used to measure the discrepancy between the distribution $p_{\mathcal{X}}(\mathbf{x})$ and the distribution learned by the generator. Training these networks involves a min-max optimization of a loss function with respect to the set of trainable parameters. In the present work, we use the Wasserstein GAN with a Gradient Penalty (WGAN-GP) [25, 26], which minimizes the Wasserstein-1 distance between $p_{\mathcal{X}}$ and the push-forward of $p_{\mathcal{Z}}$ by the generator. Since convergence of distributions in the Wasserstein-1 metric is equivalent to weak convergence [27] (Theorem 6.9), for a perfectly trained generator, \mathbf{g}^* , trained using samples from the prior distribution, $p_{\mathcal{X}}^{\text{prior}}$, we have,

$$\mathbb{E}_{\mathbf{x} \sim p_{\mathcal{X}}^{\text{prior}}(\mathbf{x})} [m(\mathbf{x})] = \mathbb{E}_{\mathbf{z} \sim p_{\mathcal{Z}}(\mathbf{z})} [m(\mathbf{g}^*(\mathbf{z}))] \quad \forall m \in C_b(\Omega_{\mathcal{X}}), \quad (4)$$

where $C_b(\cdot)$ is the space of continuous bounded functions.

Equation (4) can be converted into an expression for the posterior distribution, assuming that p_η is continuous and bounded. This is accomplished by setting $m(\cdot) = l(\cdot)p_\eta(\hat{\mathbf{y}} - \mathbf{f}(\cdot))/p_{\mathcal{Y}}(\hat{\mathbf{y}})$ in (4) where $l \in C_b(\Omega_{\mathcal{X}})$, and using (2), to arrive at

$$\mathbb{E}_{\mathbf{x} \sim p_{\mathcal{X}}^{\text{post}}(\mathbf{x})} [l(\mathbf{x})] = \mathbb{E}_{\mathbf{z} \sim p_{\mathcal{Z}}^{\text{post}}(\mathbf{z})} [l(\mathbf{g}^*(\mathbf{z}))]. \quad (5)$$

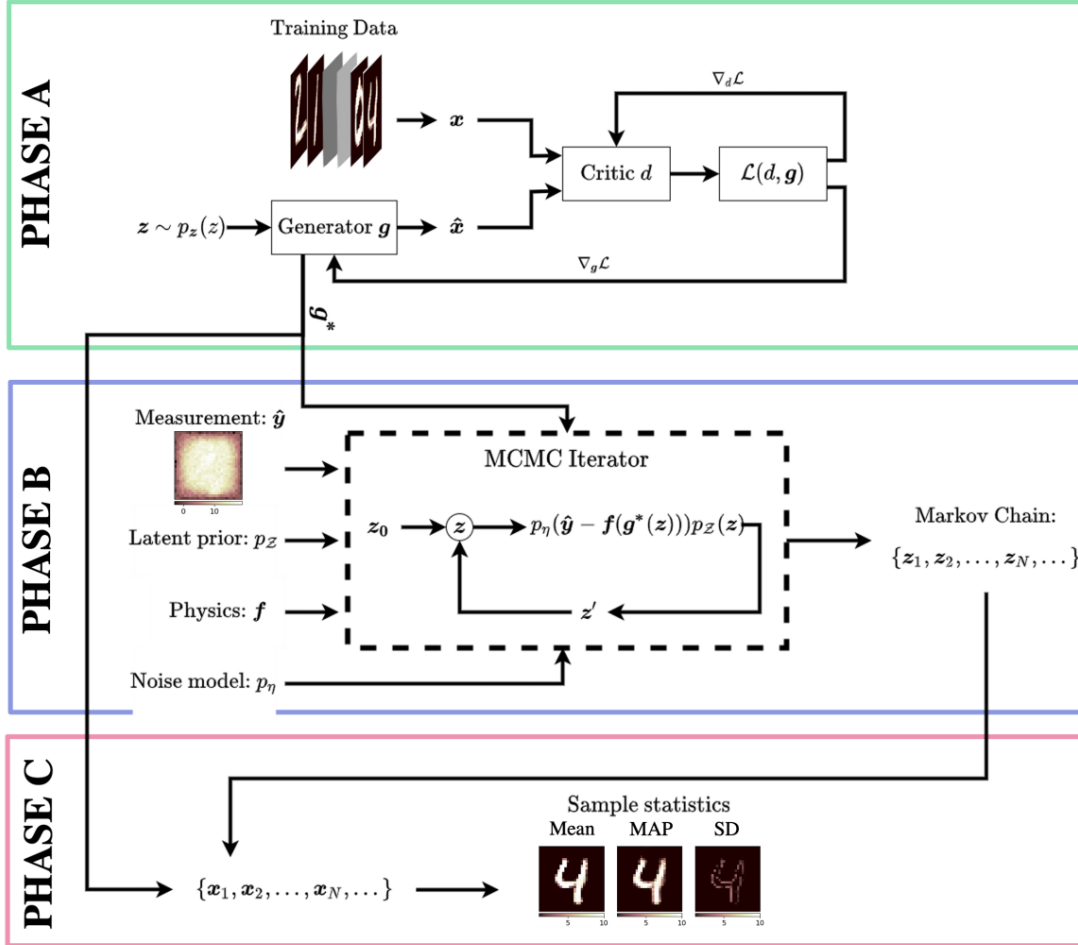


Figure 1: Schematic diagram of the inference algorithm. PHASE A: A WGAN-GP is trained using previously acquired samples of the field that is to be inferred. PHASE B: This generator, the measurement, the direct model, and the noise distribution are used in an MCMC iterator which learns the posterior distribution in latent space. PHASE C: The converged Markov chain is used to sample from the posterior distribution in the latent space and these samples are passed through the trained generator to yield samples of the inferred field.

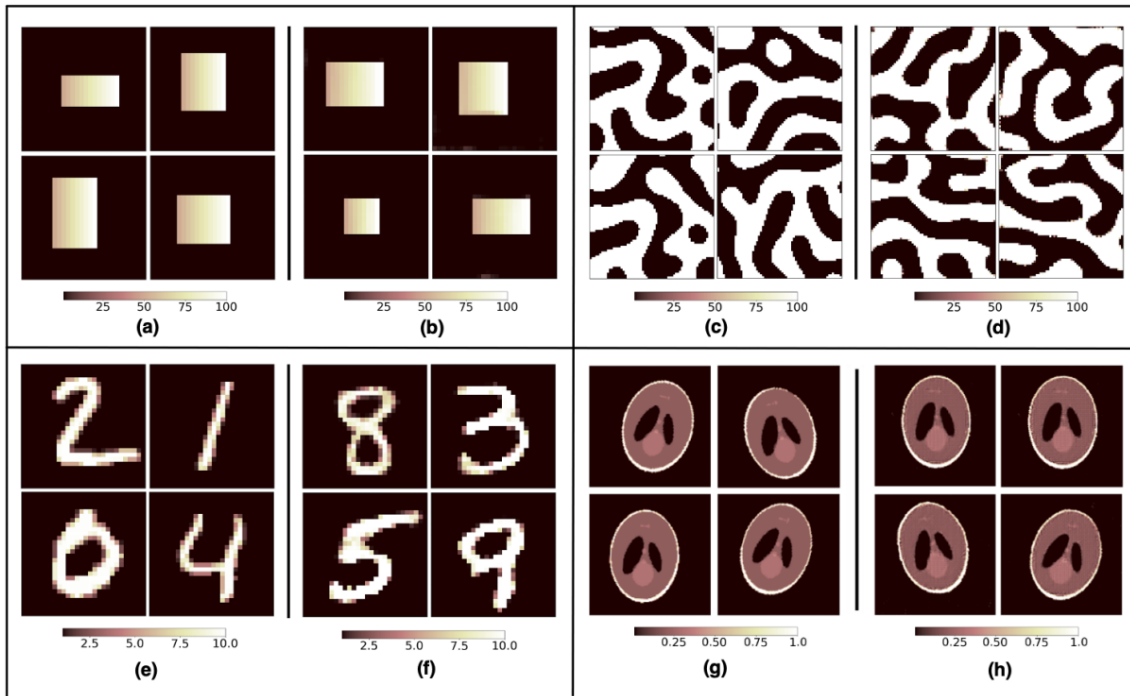


Figure 2: Typical samples from different prior distributions: (a) Parametric rectangular thermal conductivity, (c) Bi-phase material microstructure, (e) MNIST handwritten digits, (g) Shepp-Logan phantoms. The samples in (b), (d), (f) and (h) are counterparts to (a), (c), (e) and (g) respectively, generated by a WGAN-GP.

Here $p_{\mathcal{Z}}^{\text{post}}$ is the posterior distribution of \mathcal{Z} given $\hat{\mathbf{y}}$ and is defined as,

$$p_{\mathcal{Z}}^{\text{post}}(\mathbf{z}|\hat{\mathbf{y}}) \equiv \frac{p_{\eta}(\hat{\mathbf{y}} - \mathbf{f}(\mathbf{g}^*(\mathbf{z})))p_{\mathcal{Z}}(\mathbf{z})}{p_{\mathcal{Y}}(\hat{\mathbf{y}})}. \quad (6)$$

Expression (5) implies that statistics with respect to $p_{\mathcal{X}}^{\text{post}}(\mathbf{x})$ can be evaluated by sampling \mathbf{z} from $p_{\mathcal{Z}}^{\text{post}}$ and passing the samples through \mathbf{g}^* . Since the expression for $p_{\mathcal{Z}}(\mathbf{z})$ is known, and $N_{\mathcal{Z}} \ll N_{\mathcal{X}}$, we can efficiently sample from $p_{\mathcal{Z}}^{\text{post}}(\mathbf{z})$ using an MCMC algorithm.

As shown in Figure 1, the inference algorithm described above involves three phases. In Phase A, the WGAN-GP is trained using previously acquired samples of the field to be inferred. In Phase B, the trained generator, the measured field, the direct map, and the noise distribution are used to generate a Markov chain which samples from an approximation to the posterior distribution in the latent space. In Phase C, this Markov chain and the trained generator are used to generate samples to evaluate the desired QoIs (details described in Section 4).

2.3 Numerical validation and results

We consider several physics-based applications to demonstrate the effectiveness of the proposed algorithm. These can be classified based on the following criteria,

1. Direct Model: we consider the diffusion equation, the linear elasticity equation, and the Radon transform.
2. Likelihood distribution: we consider three different scenarios commonly encountered in inference problems: (a) the likelihood distribution and its parameters are known, (b) the likelihood distribution is known but its parameters are not, and (c) the likelihood distribution is not known and must be guessed, which corresponds to a real-world experimental situation wherein the underlying noise model is unknown.
3. Prior distribution: we consider five different types of prior distributions that illustrate the diversity in the class of distributions that can be approximated using a WGAN-GP.

2.3.1 Inverse heat conduction

This is a non-linear coefficient inversion problem for an elliptic PDE which arises in many fields such as subsurface flow modeling [28], electrical impedance tomography [13], and inverse heat conduction [29]. We focus on the heat conduction problem where the goal is to infer the point-wise thermal conductivity distribution, given partial and noisy measurement of temperature. The governing PDE and boundary conditions are described in Section 4.3. We consider three different types of datasets to train the prior for thermal conductivity. For each dataset, we first train a WGAN-GP to learn the prior distribution using samples from the training set. We then select samples of conductivity from the test set and solve the direct problem to determine the temperature field. We add uncorrelated Gaussian noise to this field and then use all, or a portion, of this field to solve the inverse problem. Finally, we compare the inferred results with the known conductivity field.

Rectangular dataset The conductivity has a uniform background value of unity and a rectangular inclusion whose top-left and bottom-right corners are located at (ξ_1, ξ_2) and (ξ_3, ξ_4) , respectively, where $\xi_1, \xi_4 \sim \mathcal{U}[0.2, 0.4]$ and $\xi_2, \xi_3 \sim \mathcal{U}[0.6, 0.8]$. The thermal conductivity within the inclusion varies linearly from 50 on the left edge to 100 on the right edge. All fields are represented on a 28×28 Cartesian grid. A dataset of 10^4 samples of conductivity is generated

by considering different realizations of the four ξ parameters. Representative samples from this dataset are shown in Figure 2(a), and those generated by a WGAN-GP trained using this dataset are shown in Figure 2(b) (the WGAN-GP architecture and training procedure are described in Supplementary Information). As can be observed from Figure 2 the generated samples are qualitatively similar to the true samples.

Images of two test samples of the conductivity field, along with the corresponding temperature field are shown in Figure 3(a). The noisy temperature field (with $p_\eta = \mathcal{N}(\boldsymbol{\mu} = \mathbf{0}, \boldsymbol{\Sigma} = \sigma_{\text{meas}}^2 \mathbf{1})$, where $\sigma_{\text{meas}}^2 = 1$) is used as the measurement and the algorithm from Figure 1 is used to infer the conductivity field, and compute the QoIs. These include the maximum a-posteriori (MAP) estimate, the mean, and the point-wise standard deviation (Figure 3(a)). This figure also shows the true conductivity, and the “reference” mean and standard deviation fields, which are computed by sampling the space of the four parameters, ξ . This comparison with the reference QoIs is possible only because the explicit four-dimensional representation for this conductivity field is known. The inferred MAP corresponds to the best guess for the true conductivity field. By comparing it with the true field, we conclude it is quite accurate even in the presence of significant measurement noise. In the mean field we observe that the edges of the inclusion are blurred thereby indicating the uncertainty in determining its boundaries. This is further highlighted in the plot of the standard deviation (SD) field which is elevated along the edges. A comparison of the inferred QoIs with their true counterparts verifies the accuracy of the proposed method.

MNIST dataset The conductivity field is constructed from the MNIST dataset [30] of hand-written digits by linearly scaling the image intensity to be between 1 and 10 units. All fields are represented on a 28×28 Cartesian grid. Representative samples from the true prior density of the conductivity field are shown in Figure 2(e). 5×10^4 images from this dataset are used to train the WGAN-GP, and samples from the trained generator are shown in Figure 2(f). Again, we note that the generated samples are qualitatively close to the true samples.

Measured temperature fields are generated by solving the direct problem for a conductivity field selected from the test set and then adding noise to it ($\sigma_{\text{meas}}^2 = 1$). Results are reported in Figure 3(b). The top row in this panel shows results for a measurement where the temperature field is known in the entire domain, and the bottom row shows results for a partial measurement. In both cases, by comparing the true conductivity field with the inferred MAP, we discern the ability of the proposed method in performing accurate inference with complex prior data. This is especially evident when comparing the MAP with the inferred result from a total variation diminishing (TV) prior, which is one of the more popular regularization methods for solving inverse problems. The mean and the standard deviation fields illustrate that the inference is most uncertain along the interface between the regions of high and low values of conductivity. Additional results at different levels of measurement noise are provided in Supplementary Information.

Two-phase material microstructure Multiple realizations of the the conductivity field are obtained by solving the Cahn-Hilliard equation with randomly selected initial conditions. All fields are represented on a 64×64 Cartesian grid. Figure 2(c) shows four representative samples from the training set, and Figure 2(d) shows four samples from the generator of the trained WGAN-GP.

The results of the inference problem are shown in Figure (3)(c). These include the noisy temperature field ($\sigma_{\text{meas}}^2 = 0.05$), which serves as the measurement, the MAP, the mean and the standard deviation of the reconstructed field. When comparing the MAP with the true conductivity field, we observe that the former is able to capture most of the streaky structure in the true field. However, there are local regions (indicated by red rectangles) where the MAP and the true field differ. These occur near the boundaries, where temperature is prescribed, and

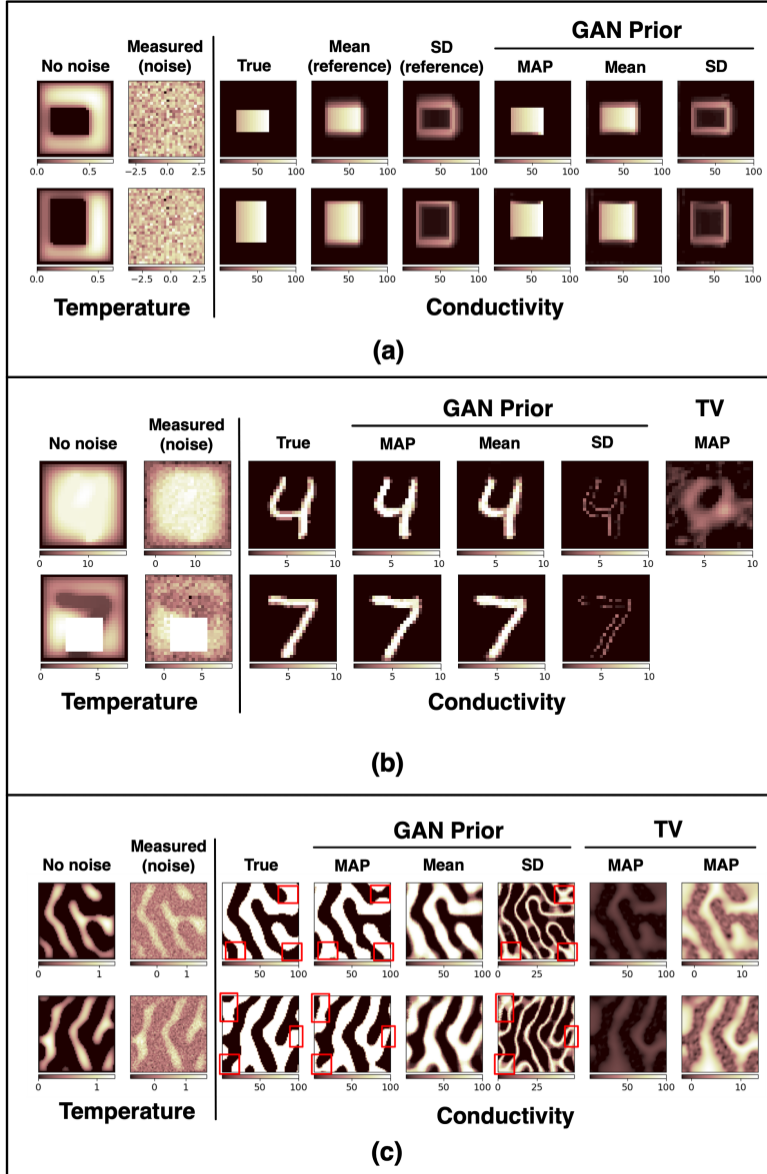


Figure 3: Results for the inverse heat conduction problem. (a) Rectangular dataset. (b) MNIST dataset. (c) Microstructure dataset.

therefore is only weakly influenced by the conductivity. Remarkably, in these regions the value of the standard deviation is elevated, clearly indicating that the uncertainty in the prediction is high, and therefore the confidence in the MAP field ought to be low. This ability to make quantitative assessments of the confidence in predictions is one of the main motivations for using probabilistic methods for solving inverse problems. A comparison of the MAP obtained using the GAN prior with the TV prior shows that the latter severely under-predicts the contrast in the conductivity field and produces oscillations that are absent from the true field.

2.3.2 Inverse Radon transform

Next, we demonstrate the efficacy of the proposed Bayesian inference strategy in the context of inverse Radon transforms, which are routinely used in computerized tomography (CT) [31]. We restrict our discussion to two-dimensional inputs (slices) scanned using one-dimensional line-Radon transforms. Given a function $\rho : \Omega \subset \mathbb{R}^2 \mapsto \mathbb{R}$, the Radon transform is given by

$$\mathcal{R}(\rho; t, \psi) := \int_{\ell_{t,\psi}} \rho d\ell, \quad (7)$$

where $\ell_{t,\psi}$ is the line through Ω inclined at an angle ψ and at a signed-distance of t from the center of Ω . For the current problem, we consider the Shepp-Logan head phantom [32], which is composed of a union of ten ellipses on the domain $\Omega = [-1.2, 1.2]^2$. The original phantom parameters are randomly perturbed to introduce variations in the phantom structure (see Section 4.4 for details).

To define the direct problem, we first obtain a discrete realization of the phantom as an image of size 128×128 . This image undergoes a further random linear transformation (see Section 4.4) to generate the input \mathbf{x} to the direct problem. Four samples of the discrete phantom are shown in Figure 2(g), where the total density at any point in the phantom ranges from 0 (air cavity) to 1 (bone). Note that the randomness in generating the samples of \mathbf{x} is attributed to the perturbation in the phantom parameters, as well as the random linear transformation of the discrete phantom.

The direct map is given by discrete Radon transforms along K^2 lines (see (19)). The resulting $K \times K$ image is known as a sinogram, an example of which is shown in Figure 4(a). A WGAN-GP is trained on a dataset with 10^4 discrete phantom images. Four realizations from the learned prior are shown in 2(h); they are qualitatively similar to the true samples. We choose a test sample from the true prior (see Figure 4 (a)), and add Gaussian noise $\mathcal{N}(\mathbf{0}, \sigma_{\text{meas}}^2 \mathbb{I})$ to the sinogram to generate the noisy measurement $\hat{\mathbf{y}}$. We then infer the underlying phantom using the algorithm in Figure 1, with the likelihood term in (2) modelled using $\mathcal{N}(\mathbf{0}, \sigma_{\text{like}}^2 \mathbb{I})$. Three different scenarios are considered for the recovery process:

Case 1: $\sigma_{\text{meas}}^2 = \sigma_{\text{like}}^2$. We assume complete knowledge of the noise model while constructing the likelihood term. Setting $K = 128$, which we term as the fine resolution, the inference results for varying levels of noise are shown in Figure 4(b). For each value of σ_{meas} , we recover the MAP estimate, mean and pixel-wise standard deviations. Even for the highest noise level in the measurement, we get an excellent recovery of the phantom, with a relatively low variance concentrated along the boundaries of the ellipses.

Case 2: $\sigma_{\text{meas}}^2 \neq \sigma_{\text{like}}^2$. We work with the same level of measurement resolution as in Case 1 and set $\sigma_{\text{meas}}^2 = 10.0$. However, we assume that we do not know the the variance of the noise. The inference results shown in Figure 4(c) with different values of σ_{like}^2 indicate a good recovery of the phantom.

Case 3: $\sigma_{\text{meas}}^2 \neq \sigma_{\text{like}}^2$ with partial observation. We consider the same situation as Case 2, but with the measurements taken at a coarser level, i.e., $K = 64$. The inference results are shown in Figure 4(d). Note that the variance along the phantom boundaries is slightly elevated compared to case 2, which is expected since the uncertainty in the results should increase with a decrease in the resolution of observed data.

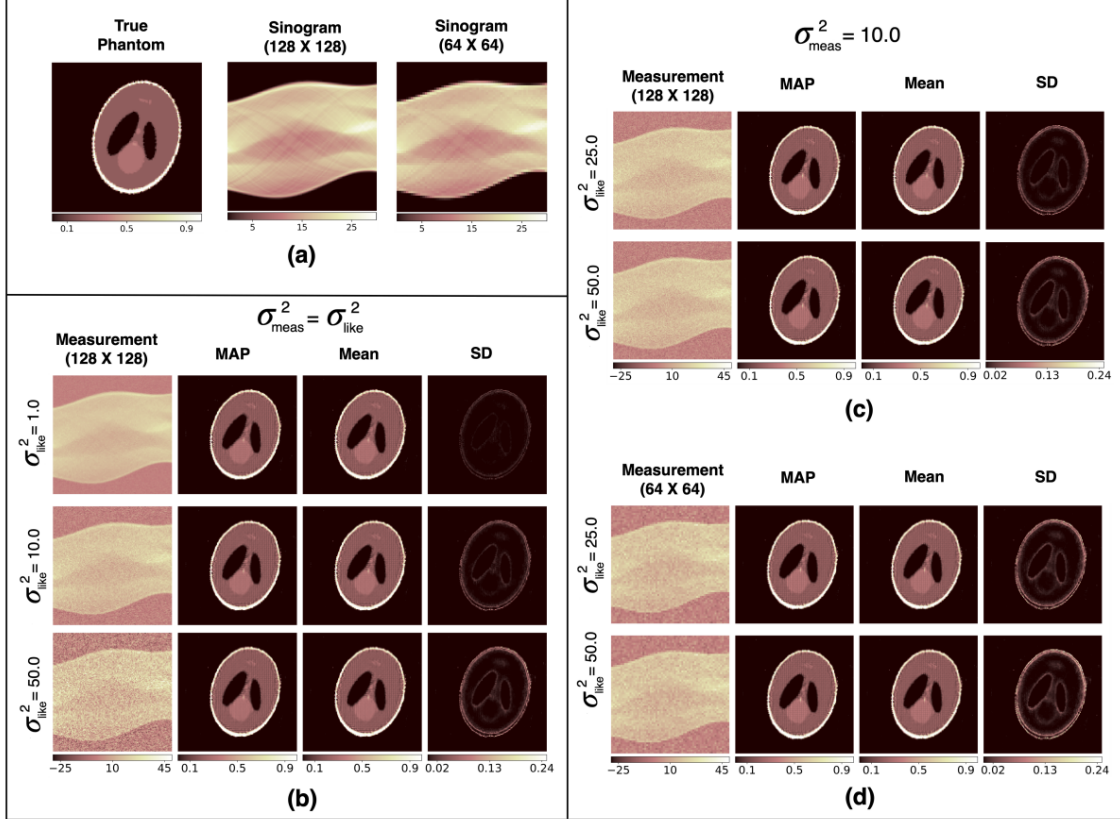


Figure 4: Results for the inverse Radon transform problem. (a) True (test) sample of the Shepp-Logan phantom and the corresponding sinograms at two different resolutions. (b) Inference results with measurements at the finer scale and when the noise level of the measurement is known precisely. (c) Inference results with measurements at the finer scale and when the noise level of the measurement is unknown. (d) Inference results with measurements at the coarser scale and when the noise level of the measurement is unknown.

2.3.3 Elasticity imaging

Elasticity imaging is a technique for inferring mechanical properties of tissue from displacement data [3, 2]. The direct problem is given by the equations of the balance of linear momentum for an incompressible linear elastic solid in a state of plane stress (see Methods Section). The corresponding inverse problem is one of determining the shear modulus given the displacement field. The data used for solving the inverse problem was obtained from a physical experiment on a tissue-mimicking phantom manufactured from a mixture of gelatin, agar, and oil [33]. The physical specimen comprised of a stiff spherical inclusion embedded in a softer background. This phantom was gently compressed and the vertical component of the displacement field in the

central plane was measured using ultrasound. This field was restricted to a rectangular domain and represented on a 56^2 grid. This grid was also used to represent the shear modulus.

In solving the inverse problem prior information about the shear modulus field was assumed. In particular, it was assumed that the field comprised a uniform circular inclusion embedded within a uniform background. The center and the size of the inclusion, and the contrast in the shear modulus between the inclusion and background, were treated as unknown parameters. A set of 6,000 realizations of the shear modulus were obtained by uniformly sampling these parameters, and was used to train a WGAN-GP to represent the prior distribution.

The measured vertical displacement field is shown in Figure 5(a). Since this field was obtained experimentally, the true model for its noise, which is needed to evaluate the likelihood term in the posterior distribution, was not known. It was assumed that the noise is Gaussian and uncorrelated and three different values of variance were used for evaluating the posterior distribution (see Figure 5). In each case, the MAP field revealed a circular inclusion with an elevated modulus, a mean field where the edge of the inclusion was blurred, and a standard deviation field that was elevated within the inclusion. The higher value of the standard deviation within the inclusion is consistent with the fact that in the stiffer regions of the phantom, a perturbation in the shear modulus leads to smaller changes in the displacement, and therefore for a spatially uniform measurement error, greater uncertainty in predictions. A quantitative comparison of the reconstructed parameters and their true counterparts is also shown in Figure 5. Here the MAP and the mean fields obtained from the reconstructions corresponding to the three different assumed noise levels were used to compute the shear modulus of the inclusion (b), the vertical coordinate of its center (c), and its diameter (d), and were compared with experimental measurements. All values were found to be within 10% of their experimental counterparts.

3 Discussion

Bayesian inference is a popular framework for solving inverse problems. However, it can be challenging to use when inferring vectors of large dimensions, and in cases where prior information is available through previously acquired samples. In this manuscript we use GANs as priors to address both these challenges. The efficacy of our approach is demonstrated on a wide range of inverse problems. These include problems where (a) the direct problem is governed by differential or integral equations, (b) the prior knowledge for the quantity to be inferred is obtained from different sources including parametric descriptions, natural images, and solutions of equations that govern the evolution of micro-structure, and (c) the likelihood distribution is known to varying degrees. In each case, in addition to evaluating the most likely value for the inferred field, we compute QoIs like the mean and standard deviation fields. These fields provide guidance to the end user by identifying regions of high uncertainty. For example, in the elasticity imaging problem considered in this paper, we observe that the largest uncertainty occurs in regions with elevated shear modulus. This is precisely where the measured displacement is most insensitive to the modulus. Similarly, in the heat conduction problem with micro-structure, the largest uncertainty occurs along the boundaries of the domain where the temperature values are determined by primarily the boundary conditions and not the thermal conductivity field.

We end with a discussion of the limitations of the approach discussed in this manuscript. First, it is applicable when a sufficiently large data set of previously acquired samples of the inferred field is available. While this may be available for some cases (like the micro-structure, and MNIST problems) and could be generated for some other problems (like the elasticity imaging and the radon transform problems), there are scenarios where this may not be possible. For these cases, other means of describing the prior ought to be considered. Second, using this approach involves training a WGAN-GP in the first phase and an MCMC sampler in the second phase.

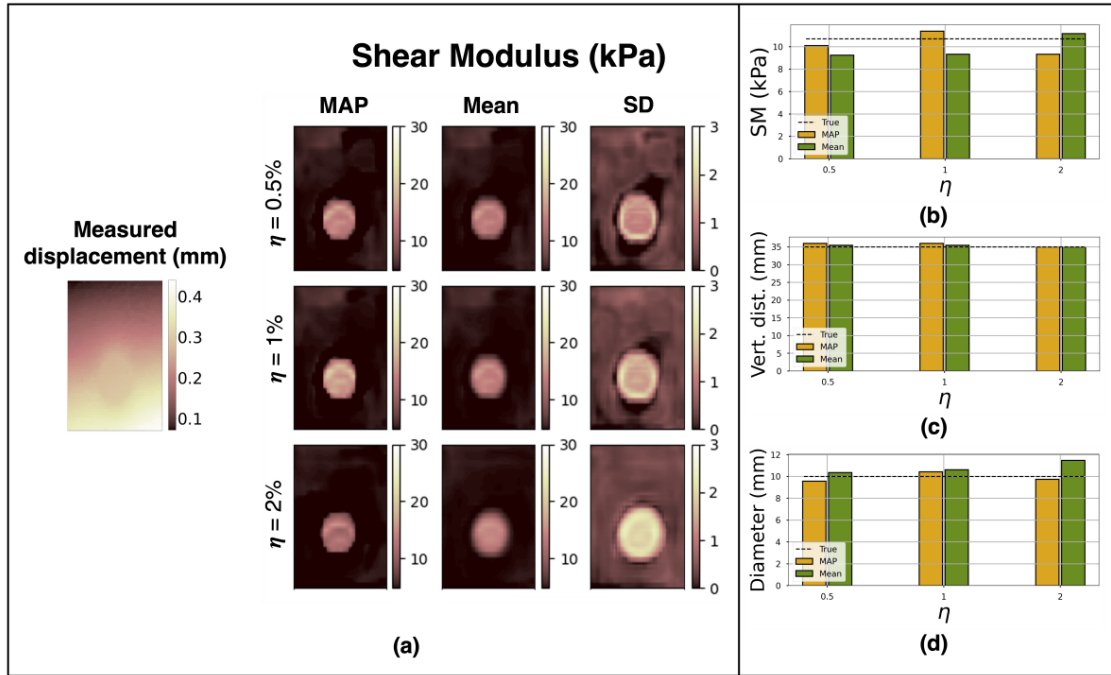


Figure 5: Results for the Elasticity Imaging problem. (a) From left to right: vertical displacement field measured in the phantom, MAP, Mean and Standard Deviation field obtained by solving the inverse problem. Each row corresponds to a different value of assumed variance in noise. (b) Shear modulus of the inclusion evaluated using the MAP and Mean fields. (c) Vertical coordinate of the center of the inclusion evaluated using the MAP and Mean fields. (d) Diameter of the inclusion evaluated using the MAP and Mean fields.

Both these tasks require careful consideration of the type of problem being solved, and the values of the hyper-parameters to be selected.

4 Methods

4.1 Generative Adversarial Networks

A number of GAN models have been developed over the years, and differ from each other on the basis of their loss function (see [15, 34, 35] for example). In order to use a GAN as a prior in Bayesian inference, the weak convergence of the density induced by the generator of the GAN to the true density is required. The Wasserstein GAN (WGAN) [25], which minimizes the Wasserstein-1 distance between these two densities, satisfies this key property and is therefore used in this work. Specifically, we use the improved version of the WGAN with a Gradient Penalty (WGAN-GP) [26], whose loss function is given by

$$\mathcal{L}(d, \mathbf{g}) = \mathbb{E}_{\mathbf{x} \sim p_{\mathcal{X}}(\mathbf{x})} [d(\mathbf{x})] - \mathbb{E}_{\mathbf{z} \sim p_{\mathcal{Z}}(\mathbf{z})} [d(\mathbf{g}(\mathbf{z}))] + \lambda \underbrace{\mathbb{E}_{\hat{\mathbf{x}} \sim \hat{p}_{\mathcal{X}}(\mathbf{x})} [(\|\nabla_{\hat{\mathbf{x}}} d(\hat{\mathbf{x}})\|_2 - 1)^2]}_{\text{gradient penalty}}. \quad (8)$$

In (8), the first term is the expectation of discriminator over the set of true samples, the second term is the expectation over the set of fake samples, λ is the penalty parameter and $\hat{p}_{\mathcal{X}}(\mathbf{x})$ defines a uniform sampling along straight lines between pairs of points sampled from $p_{\mathcal{X}}(\mathbf{x})$ and the push-forward of $p_{\mathcal{Z}}(\mathbf{z})$ by \mathbf{g} . The gradient penalty constrains the discriminator to be a 1-Lipschitz function. The WGAN-GP is trained by solving the following min-max problem,

$$(d^*, \mathbf{g}^*) = \arg \min_d \arg \max_{\mathbf{g}} \mathcal{L}(d, \mathbf{g}). \quad (9)$$

As described in [25, 26], the inner maximization problem under the Lipschitz constraint on the discriminator leads to an approximation of the Wasserstein-1 distance between $p_{\mathcal{X}}$ and the push-forward of $p_{\mathcal{Z}}$ by a given generator. The outer minimization problem corresponds to finding a generator that minimizes this Wasserstein-1 distance. In our work, we use the WGAN-GP such that the push-forward of $p_{\mathcal{Z}}$ approximates the prior distribution.

4.2 Expression for QoIs and the MAP estimate

In this section we describe how Equation (5) can be utilized to compute some specific QoIs and the maximum a-posteriori (MAP) estimate.

Mean An estimate of the mean of the posterior distribution, $p_{\mathcal{X}}^{\text{post}}(\mathbf{x}|\hat{\mathbf{y}})$, can be computed by using $l(\mathbf{x}) = \mathbf{x}$ in Equation (5). That is

$$\bar{\mathbf{x}} = \mathbb{E}_{\mathbf{x} \sim p_{\mathcal{X}}^{\text{post}}} [\mathbf{x}] = \mathbb{E}_{\mathbf{z} \sim p_{\mathcal{Z}}^{\text{post}}} [\mathbf{g}^*(\mathbf{z})]. \quad (10)$$

Standard deviation In order to compute the standard deviation estimate with respect to the posterior distribution, we first compute the second moment,

$$\bar{\mathbf{m}} = \mathbb{E}_{\mathbf{x} \sim p_{\mathcal{X}}^{\text{post}}} [\mathbf{x}^2] = \mathbb{E}_{\mathbf{z} \sim p_{\mathcal{Z}}^{\text{post}}} [(\mathbf{g}^*(\mathbf{z}))^2], \quad (11)$$

where the square of a vector is understood to be the square of each of its components. Thereafter, we use the mean and the second moment to evaluate the component-wise standard deviation,

$$\boldsymbol{\sigma} = \sqrt{\bar{\mathbf{m}} - \bar{\mathbf{x}}^2}. \quad (12)$$

MAP Estimate Since the explicit expression for the prior $p_{\mathcal{X}}^{\text{prior}}(\mathbf{x})$ is not known, it is not possible to use Equation (2) to determine the value of the posterior distribution (even up to a multiplicative constant). Therefore, it is not possible to directly determine the MAP estimate, \mathbf{x}^{MAP} , within our approach. However, it is possible to estimate \mathbf{z}^{MAP} using the expression for $p_{\mathcal{Z}}^{\text{post}}(\mathbf{z}|\hat{\mathbf{y}})$ (Equation (13)). For every sample generated by the MCMC chain, we evaluate the log of this distribution (up to an additive constant), and of those, designate the sample with the largest value as \mathbf{z}^{MAP} . Thereafter we treat $\mathbf{g}^*(\mathbf{z}^{\text{MAP}})$ as an approximation to \mathbf{x}^{MAP} .

In the special case of additive Gaussian noise and Gaussian latent distribution, \mathbf{z}^{MAP} can be determined using a simple optimization algorithm. We consider the case when the components of the latent vector are i. i. d. sampled from a normal distribution with zero mean and unit variance. This is often the case in many typical GAN applications. Further, we assume that the components of the noise vector are defined by a normal distribution with zero mean and a covariance matrix Σ . Using these assumptions in (6), we have

$$p_{\mathcal{Z}}^{\text{post}}(\mathbf{z}|\hat{\mathbf{y}}) \propto \exp\left(-\frac{1}{2}\overbrace{(|\Sigma^{-1/2}(\hat{\mathbf{y}} - \mathbf{f}(\mathbf{g}^*(\mathbf{z})))|^2 + |\mathbf{z}|^2)}^{\equiv r(\mathbf{z})}\right). \quad (13)$$

The MAP estimate for this distribution is obtained by minimizing the negative of the argument of the exponential. That is

$$\mathbf{z}^{\text{MAP}} = \arg \min_{\mathbf{z}} r(\mathbf{z}). \quad (14)$$

4.3 Inverse heat conduction

For this problem the forward model is described by the steady-state heat conduction equation:

$$\begin{aligned} -\nabla \cdot (\kappa(\mathbf{s})\nabla u(\mathbf{s})) &= b(\mathbf{s}), & \mathbf{s} &= (s_1, s_2) \in \Omega \\ u(\mathbf{s}) &= 0, & \mathbf{s} &= (s_1, s_2) \in \partial\Omega \end{aligned} \quad (15)$$

where $\Omega \subset \mathbb{R}^2$ is a square domain with length = 1 unit, and $b(\mathbf{s}) = 10^3$ denotes the heat source. The goal is to infer the posterior QoIs of conductivity field κ , given a noisy, and potentially partial, measurement of temperature field u . The nodal values of the temperature field are stored in the vector \mathbf{y} and those of the conductivity field are stored in the vector \mathbf{x} .

We compute different QoIs (such as mean, standard deviation etc.) with respect to posterior distribution using the method proposed in the manuscript and expressions for QoIs shown above. Reference QoIs are calculated using random sampling.

4.4 Shepp-Logan phantom dataset and the forward problem

The Shepp-Logan phantom is composed of a union of ten ellipses with each ellipse having a different but constant density. The k -th ellipse E_k is centered at (r_k, s_k) , with semi-axis lengths a_k, b_k , angle of inclination α_k and density ρ_k . The precise values of these parameters having been taken from [32] and are also tabulated in the supplementary material. To generate training and test samples, the original parameters are randomly sampled to obtain a perturbed ellipse \tilde{E}_k as follows:

$$\begin{aligned} \tilde{r}_k &= r_k + 0.005\omega_k^1, & \tilde{s}_k &= s_k + 0.005\omega_k^2, & \tilde{a}_k &= a_k + 0.005\omega_k^3, \\ \tilde{b}_k &= b_k + 0.005\omega_k^4, & \tilde{\alpha}_k &= \alpha_k + 2.5\omega_k^5, & \tilde{\rho}_k &= \rho_k + 0.0005\omega_k^6. \end{aligned} \quad (16)$$

The random parameters in (16) are sampled uniformly as $\omega_k^i \sim \mathcal{U}[-1, 1]$. The density ρ for the perturbed Shepp-Logan phantom is given by

$$\rho(r, s) = \max \left(0, \min \left(1, \sum_{k=1}^{10} \tilde{C}_k(r, s) \right) \right), \quad \tilde{C}_k(r, s) = \begin{cases} \rho_k & \text{if } (r, s) \in \tilde{E}_k \\ 0 & \text{otherwise} \end{cases} \quad (17)$$

The clipping in (17) ensures that the total density at any point in the phantom ranges from 0 (air cavity) to 1 (bone).

The discrete phantom \mathbf{x} obtained by evaluating (17) on a grid of 128×128 . This phantom image is further transformed as $\mathbf{x} \leftarrow \mathcal{F}(\mathbf{x}; n, m, \beta)$ to generate a single training (or test) sample. The transformation \mathcal{F} translates \mathbf{x} by n pixels in the horizontal direction, m pixels in the vertical direction and rotates by an angle β , where

$$n, m \sim \mathcal{U}\{-8, -7, \dots, 7, 8\}, \quad \beta \sim \mathcal{U}[-20^\circ, 20^\circ]. \quad (18)$$

The forward map for the problem is given by

$$\begin{aligned} \mathbf{f}(\mathbf{x}) &= \mathbf{y} \in \mathbb{R}^{K \times K}, \\ y_{i,j} &= \mathcal{R}^h(\mathbf{x}; t_i, \psi_j), \\ t_i &= \frac{i}{K}, \quad \forall 1 \leq i \leq K, \\ \psi_j &= \frac{j}{\pi}, \quad \forall 1 \leq j \leq K, \end{aligned} \quad (19)$$

where the discrete Radon transform \mathcal{R}^h along each of the K^2 lines is computed using a quadrature.

4.5 Elasticity imaging

The forward problem is given by the equations of the balance of linear momentum for an incompressible linear elastic solid in a state of plane stress,

$$\begin{aligned} \nabla \cdot \boldsymbol{\sigma} &= \mathbf{0} && \text{in } \Omega \\ \mathbf{u} &= \mathbf{u}_D && \text{on } \Gamma_D \\ \boldsymbol{\sigma} \cdot \mathbf{n} &= \boldsymbol{\tau} && \text{on } \Gamma_N \end{aligned} \quad (20)$$

where $\boldsymbol{\sigma} = 2\mu(\nabla^s \mathbf{u} + (\nabla \cdot \mathbf{u})\mathbf{1})$ is the stress tensor, μ is the shear modulus, and \mathbf{u} is the displacement field. In the problem considered in the study, the domain Ω is a rectangle of dimension $34.608 \times 26.297 \text{ mm}$. On the vertical edges of the rectangle, a zero traction boundary condition is prescribed, whereas on the horizontal edges the vertical displacement is set equal to its measured vertical value and horizontal traction is set to zero. The nodal values of the vertical displacement and the nodal values of the shear modulus constitute the measurement vector \mathbf{y} , and inferred vector \mathbf{x} , respectively. The inverse problem is one of determining the shear modulus given the vertical displacement field.

4.6 WGAN-GP architecture and MCMC sampler

In all numerical experiments the Wasserstein GAN-GP model is used to learn the prior density (phase A of Figure 1). The details regarding the architecture of the WGAN-GP, the number of training samples, and the corresponding hyper-parameters used in different numerical experiments are provided in the supplementary material. The target images used for posterior inference are not selected from the training set used to train the WGAN. All WGAN models are trained using

TensorFlow [36]. The trained WGAN generator \mathbf{g}^* is used in conjunction with the measured field \mathbf{x} , the known forward model \mathbf{f} and the likelihood distribution p_η to perform the posterior sampling (phase B of Figure 1). For this purpose the Hamiltonian Monte Carlo (HMC) is used due to its superior convergence properties (implemented in TensorFlow Probability [37]). An initial step size of 1.0 is used for the HMC sampler, and is adapted based on the target acceptance probability [38]. The hyper-parameters used for the HMC sampler are provided in the supplementary material. All PDE-based forward problems are solved using the finite element methods using FEniCS [39] library.

5 Acknowledgements

The authors acknowledge support from ARO grant W911NF2010050 and from the Airbus Institute for Engineering Research at USC. The authors acknowledge the Center for Advanced Research Computing (CARC) at the University of Southern California for providing computing resources that have contributed to the research results reported within this publication.

6 Author Contributions

DP and AAO developed the mathematical formulation. DP and DR implemented the computational algorithms. DP generated results for the heat conduction and elastography problems, and DR generated results for the Radon transform problem. All authors contributed to the writing and editing of the manuscript.

7 Competing Interests statement

The authors have no competing interests to declare.

References

- [1] J. B. Keller, “Inverse problems,” *The American Mathematical Monthly*, vol. 83, no. 2, pp. 107–118, 1976.
- [2] M. M. Doyley and K. J. Parker, “Elastography: general principles and clinical applications,” *Ultrasound clinics*, vol. 9, no. 1, p. 1, 2014.
- [3] P. E. Barbone and A. A. Oberai, “A review of the mathematical and computational foundations of biomechanical imaging,” in *Computational Modeling in Biomechanics*, pp. 375–408, Springer, 2010.
- [4] A. Kirsch, *An introduction to the mathematical theory of inverse problems*, vol. 120. Springer Nature, 2021.
- [5] V. Isakov, *Inverse problems for partial differential equations*, vol. 127. Springer, 2006.
- [6] R. Snieder and J. Trampert, “Inverse Problems in Geophysics,” pp. 119–190, Springer, Vienna, 1999.
- [7] W. P. Gouveia and J. A. Scales, “Resolution of seismic waveform inversion: Bayes versus Occam,” *Inverse Problems*, vol. 13, pp. 323–349, apr 1997.

- [8] C. Jackson, M. K. Sen, P. L. Stoffa, C. Jackson, M. K. Sen, and P. L. Stoffa, “An Efficient Stochastic Bayesian Approach to Optimal Parameter and Uncertainty Estimation for Climate Model Predictions,” *Journal of Climate*, vol. 17, pp. 2828–2841, jul 2004.
- [9] S. Huang, J. Xiang, H. Du, and X. Cao, “Inverse problems in atmospheric science and their application,” *Journal of Physics: Conference Series*, vol. 12, pp. 45–57, jan 2005.
- [10] I. Craig and J. C. Brown, “Inverse problems in astronomy, a guide to inversion strategies for remotely sensed data,” 1986.
- [11] A. Asensio Ramos, M. J. Martínez González, and J. A. Rubiño-Martín, “Bayesian inversion of Stokes profiles,” *Astronomy & Astrophysics*, vol. 476, pp. 959–970, dec 2007.
- [12] J. Hadamard, “Sur les problèmes aux dérivées partielles et leur signification physique,” *Princeton university bulletin*, pp. 49–52, 1902.
- [13] J. Kaipio and E. Somersalo, *Statistical and computational inverse problems*, vol. 160. Springer Science & Business Media, 2006.
- [14] M. Dashti and A. M. Stuart, “The bayesian approach to inverse problems,” *Handbook of Uncertainty Quantification*, pp. 1–118, 2016.
- [15] I. Goodfellow, J. Pouget-Abadie, M. Mirza, B. Xu, D. Warde-Farley, S. Ozair, A. Courville, and Y. Bengio, “Generative adversarial nets,” in *Advances in neural information processing systems*, pp. 2672–2680, 2014.
- [16] J. Adler and O. Öktem, “Deep bayesian inversion,” *arXiv preprint arXiv:1811.05910*, 2018.
- [17] Y. Yang and P. Perdikaris, “Adversarial uncertainty quantification in physics-informed neural networks,” *Journal of Computational Physics*, vol. 394, pp. 136–152, 2019.
- [18] D. V. Patel and A. A. Oberai, “Gan-based priors for quantifying uncertainty,” *arXiv preprint arXiv:2003.12597*, 2020.
- [19] M. Vauhkonen, J. P. Kaipio, E. Somersalo, and P. A. Karjalainen, “Electrical impedance tomography with basis constraints,” *Inverse Problems*, vol. 13, pp. 523–530, apr 1997.
- [20] D. Calvetti and E. Somersalo, “Priorconditioners for linear systems,” *Inverse Problems*, vol. 21, pp. 1397–1418, aug 2005.
- [21] W. Li and O. A. Cirpka, “Efficient geostatistical inverse methods for structured and unstructured grids,” *Water Resources Research*, vol. 42, jun 2006.
- [22] Y. M. Marzouk and H. N. Najm, “Dimensionality reduction and polynomial chaos acceleration of Bayesian inference in inverse problems,” *Journal of Computational Physics*, vol. 228, pp. 1862–1902, apr 2009.
- [23] C. Lieberman, K. Willcox, and O. Ghattas, “Parameter and State Model Reduction for Large-Scale Statistical Inverse Problems,” *SIAM Journal on Scientific Computing*, vol. 32, pp. 2523–2542, jan 2010.
- [24] S. Brooks, A. Gelman, G. L. Jones, and X. L. Meng, *Handbook of Markov Chain Monte Carlo*. CRC Press, may 2011.

- [25] M. Arjovsky, S. Chintala, and L. Bottou, “Wasserstein generative adversarial networks,” in *Proceedings of the 34th International Conference on Machine Learning* (D. Precup and Y. W. Teh, eds.), vol. 70 of *Proceedings of Machine Learning Research*, (International Convention Centre, Sydney, Australia), pp. 214–223, PMLR, 06–11 Aug 2017.
- [26] I. Gulrajani, F. Ahmed, M. Arjovsky, V. Dumoulin, and A. C. Courville, “Improved training of wasserstein gans,” in *Advances in neural information processing systems*, pp. 5767–5777, 2017.
- [27] C. Villani, *Optimal Transport: Old and New*. Grundlehren der mathematischen Wissenschaften, Springer Berlin Heidelberg, 2008.
- [28] M. Iglesias, K. Law, and A. Stuart, “Evaluation of Gaussian approximations for data assimilation in reservoir models,” *Computational Geosciences*, vol. 17, pp. 851–885, 2013.
- [29] J. P. Kaipio and C. Fox, “The Bayesian Framework for Inverse Problems in Heat Transfer,” *Heat Transfer Engineering*, vol. 32, no. 9, pp. 718–753, 2011.
- [30] Y. LeCun, C. Cortes, and C. Burges, “Mnist handwritten digit database,” *ATT Labs [Online]*. Available: <http://yann.lecun.com/exdb/mnist>, vol. 2, 2010.
- [31] F. Natterer, *The Mathematics of Computerized Tomography*. Society for Industrial and Applied Mathematics, 2001.
- [32] P. A. Toft, *The Radon Transform - Theory and Implementation*. PhD thesis, Technical University of Denmark, 1996.
- [33] T. Z. Pavan, E. L. Madsen, G. R. Frank, J. Jiang, A. A. Carneiro, and T. J. Hall, “A nonlinear elasticity phantom containing spherical inclusions,” *Physics in Medicine and Biology*, vol. 57, pp. 4787–4804, aug 2012.
- [34] B. Poole, A. A. Alemi, J. Sohl-Dickstein, and A. Angelova, “Improved generator objectives for gans,” 2016.
- [35] S. Nowozin, B. Cseke, and R. Tomioka, “f-gan: Training generative neural samplers using variational divergence minimization,” 2016.
- [36] M. Abadi, A. Agarwal, P. Barham, E. Brevdo, Z. Chen, C. Citro, G. S. Corrado, A. Davis, J. Dean, M. Devin, S. Ghemawat, I. Goodfellow, A. Harp, G. Irving, M. Isard, Y. Jia, R. Jozefowicz, L. Kaiser, M. Kudlur, J. Levenberg, D. Mané, R. Monga, S. Moore, D. Murray, C. Olah, M. Schuster, J. Shlens, B. Steiner, I. Sutskever, K. Talwar, P. Tucker, V. Vanhoucke, V. Vasudevan, F. Viégas, O. Vinyals, P. Warden, M. Wattenberg, M. Wicke, Y. Yu, and X. Zheng, “TensorFlow: Large-scale machine learning on heterogeneous systems,” 2015. Software available from tensorflow.org.
- [37] J. V. Dillon, I. Langmore, D. Tran, E. Brevdo, S. Vasudevan, D. Moore, B. Patton, A. Alemi, M. Hoffman, and R. A. Saurous, “TensorFlow Distributions,” nov 2017.
- [38] C. Andrieu and J. Thoms, “A tutorial on adaptive MCMC,” *Statistics and Computing*, vol. 18, pp. 343–373, dec 2008.
- [39] M. S. Alnaes, J. Blechta, J. Hake, A. Johansson, B. Kehlet, A. Logg, C. Richardson, J. Ring, M. E. Rognes, and G. N. Wells, “The FEniCS Project Version 1.5,” *The FEniCS Project Version 1.5*, vol. 3, pp. 9–23, dec 2015.

Supplementary Information

1 Datasets

In this section we provide details about datasets used in different numerical experiments. We explain details of how different datasets were generated and the values of associated parameters.

1.1 Rectangular dataset

The rectangular dataset consists of a rectangular patch with linearly varying conductivity with a background with constant conductivity. The background conductivity value is set to 1 and the value inside rectangular patch varies from 50 (on left edge) to 100 (on right edge of rectangle).

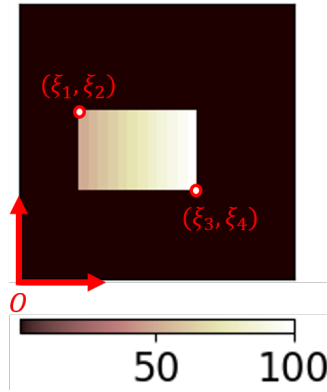


Figure 1: Parametric description of rectangular dataset.

As can be observed from Figure 1, this dataset can be parametrized by the four parameters $\xi_1, \xi_2, \xi_3, \xi_4$. Each of these parameters are sampled from uniform distribution. Specifically, $\xi_1 \sim \mathcal{U}[0.2, 0.4] * L$, $\xi_2 \sim \mathcal{U}[0.6, 0.8] * L$, $\xi_3 \sim \mathcal{U}[0.2, 0.4] * L$ and $\xi_4 \sim \mathcal{U}[0.6, 0.8] * L$, where $L=1$ unit.

1.2 Original Shepp-Logan phantom

The Shepp-Logan phantom is composed of a union of ten ellipses. The k -th ellipse E_k (see Figure 2) is centered at (r_k, s_k) , with semi-axis lengths a_k, b_k and angle of inclination α_k . The density inside this ellipse is given by a constant $\rho_k > 0$, while the density outside the ellipse is 0. The base parameter values of each ellipse is listed in Table 1. The density of the phantom at any coordinate (r, s) is given by

$$\rho(r, s) = \sum_{k=1}^{10} C_k(r, s), \quad C_k(r, s) = \begin{cases} \rho_k & \text{if } (r, s) \in E_k \\ 0 & \text{otherwise} \end{cases} \quad (1)$$

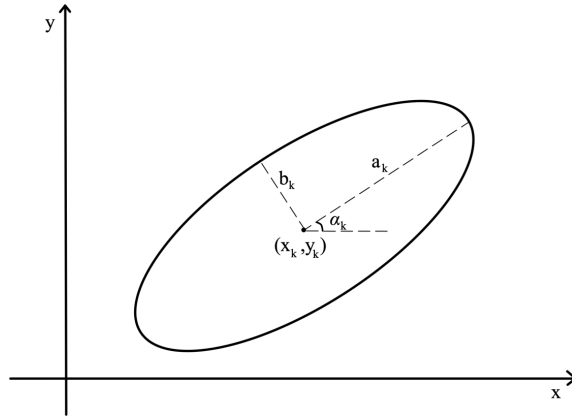


Figure 2: Ellipse used to construct the Shepp-Logan phantom.

k	r_k	s_k	a_k	b_k	α_k (degrees)	ρ_k
1	0.0	0.0	0.69	0.92	0	1.0
2	0.0	-0.0184	0.6624	0.874	0	-0.8
3	0.22	0.0	0.11	0.31	-18	-0.2
4	-0.22	0.0	0.16	0.41	-18	-0.2
5	0.0	0.35	0.21	0.25	0	0.1
6	0.0	0.1	0.046	0.026	0	0.1
7	0.0	-0.1	0.046	0.046	0	0.1
8	-0.08	-0.605	0.046	0.023	0	0.1
9	0.0	-0.606	0.023	0.023	0	0.1
10	0.06	-0.605	0.023	0.046	0	0.1

Table 1: Base parameters for Shepp-Logan head phantom.

1.3 Circular phantom dataset

For the elastography experiment described in the Results section we use circular phantom dataset. This dataset (of shear modulus field) was synthetically generated by varying three parameters: x and y -coordinate of the center of the circular inclusion and the ratio of the shear modulus value inside the inclusion to shear modulus value outside the inclusion. The total domain size is 34.608 mm in x -direction and 26.287 mm in y -direction. x -coordinate and y -coordinates were sampled from $\mathcal{U}[7.30, 19.96]\text{ mm}$ and $\mathcal{U}[7.4, 25.96]\text{ mm}$. The ratio of shear modulus value was sampled from $\mathcal{U}[1, 8]$ with background value of shear modulus set to 4.7 kPa . The choice of the shape of the inclusion and the values of three parameters were made based on the prior knowledge about the experiment. This simulates many real-world scenarios where, based on prior domain knowledge, one selects the appropriate *prior* distribution.

2 Computing the TV solution

We compare the MAP estimate obtained from our approach with the optimal solution (denoted by \mathbf{x}^*) obtained by solving a deterministic inverse problem with Total Variation (TV) regularization, which is a gold-standard regularizer for physics-driven inverse problems. Specifically, we compute \mathbf{x}^* by solving following optimization problem,

$$\mathbf{x}^* = \frac{1}{2} \int_{\Omega} (\hat{\mathbf{y}} - \mathbf{f}(\mathbf{x}))^2 d\mathbf{y} + \frac{\gamma}{2} \int_{\Omega} \sqrt{(\nabla \mathbf{x})^2 + \epsilon} d\mathbf{x}, \quad (2)$$

where γ is the regularization parameter, ϵ is total variation parameter that ensures continuous derivatives at $\mathbf{x} = \mathbf{0}$, and ∇ denotes an approximation to the gradient of the spatial field represented by \mathbf{x} .

We solve the above optimization problem using inexact Hessian-free Newton-Conjugate Gradient (CG) method following the strategy described in [1]. The main components of this method are as follows:

- The method approximately solves the linear system stemming from each Newton iteration of the optimization problem described in equation (2) using the conjugate gradient method.
- The Newton system is solved inexactly by early termination of CG iterations via Eisenstat-Walker and Steihaug criteria.
- The method does not require explicit calculation of expensive Hessian matrix for Newton iterations. Instead it requires first solving the forward and adjoint problems to compute the gradient, and then incremental forward and incremental adjoint problems to compute the action of Hessian on gradient.
- The step size for the optimization algorithm is selected by Armijo backtracking line search.
- The value of the regularization parameter γ is selected based on the L-curve criteria and the value of TV parameter ϵ is set to $1e - 4$.

3 Additional Results

3.1 Effect of noise level on reconstruction results

An inference algorithm in Bayesian setting should perform consistently across different noise levels in measured field. This ensures that the obtained results are robust and reliable. To investigate

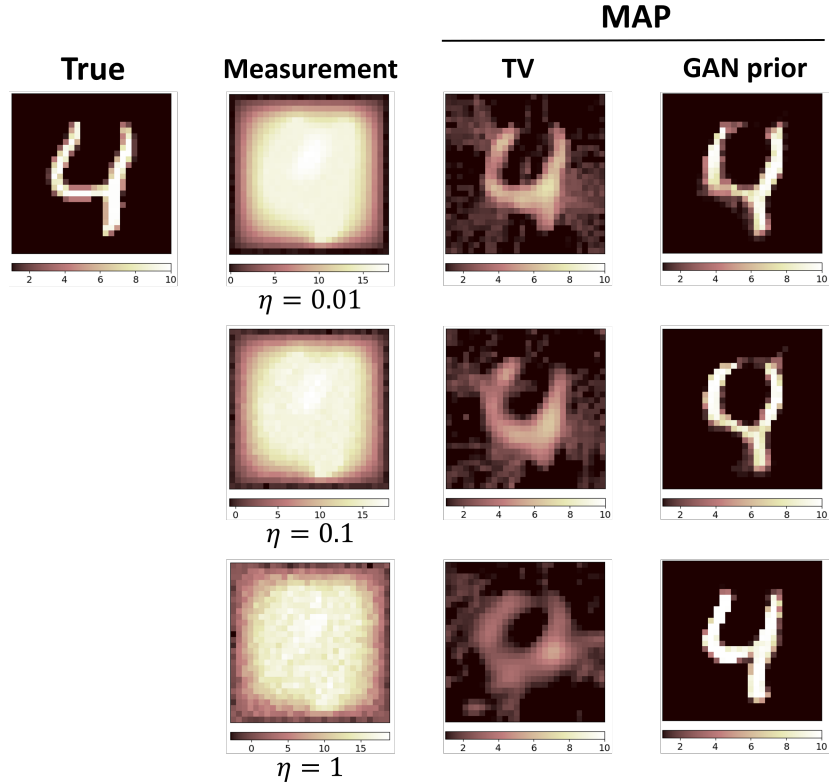


Figure 3: Effect of measurement noise on reconstruction results. *First column*: true conductivity field from test set. *Second column*: temperature measurements with different level of additive Gaussian noise. *Third column*: reconstruction results obtained by solving deterministic optimization problem with TV regularization. *Fourth column*: MAP estimate obtained from our proposed GAN prior method.

this, in this section, we study the effect of noise level on reconstruction results obtained by our algorithm and compare it against reconstruction obtained from TV regularization. We consider the thermal conductivity inversion problem (described in the Results section) and use MNIST dataset.

Figure 3 shows the results of this study showcasing the effect of measurement noise on reconstruction quality. Second column of Figure 3 shows temperature field corrupted with measurement noise. (For this study we consider additive Gaussian noise as our noise model for measured field with three different noise variance: 0.01, 0.1, and 1.0). Last two columns represent reconstruction results for TV regularization and our proposed algorithm. As can be observed, GAN-based priors perform significantly better than TV at all noise levels. Furthermore, the performance of our method stays consistent even at very high noise level ($\eta = 1$), whereas the performance of TV method degrades significantly. This should not be surprising, since our method learns prior directly from data and hence uses prior density which is more close to “true” prior density, whereas TV method uses pre-defined analytical form of regularization promoting piece-wise constant solution, which might not necessarily be the optimal choice. This highlights a key feature of our proposed method: using a prior density, which is learned directly from data, leads to stronger priors which enables better posterior approximation even in the presence of high measurement noise.

We note that the important hyperparameters of TV method, such as regularization parameter, were optimally tuned using L-curve criteria [2] to ensure fair comparison.

3.2 Inverse heat conduction : source identification

In this section we consider a different inverse problem that may arise in steady state diffusion equation - the one of inferring source term from temperature measurement. We note that this inverse problem is severely ill-posed and more challenging to solve than thermal conductivity inversion due to significant information loss in measured field because of the Laplacian operator. Such inverse source identification problems are becoming increasingly important in various areas of science and engineering, for example, an accurate estimation of pollutant source is critical in designing safe systems. Such inverse problems also play crucial role in the design and development of thermal equipments and systems and hence they have garnered significant research attention in the last couple of decades [3, 4, 5, 6].

Let us consider the steady-state diffusion equation

$$\begin{aligned}
 -\nabla \cdot (\kappa(\mathbf{s})\nabla u(\mathbf{s})) &= b(\mathbf{s}), & \mathbf{s} &= (s_1, s_2) \in \Omega \\
 u(\mathbf{s}) &= 0, & \mathbf{s} &= (0, s_2) \cup (L, s_2) \in \partial\Omega_g \\
 \frac{\partial u(\mathbf{s})}{\partial \mathbf{s}} &= 0, & \mathbf{s} &= (s_1, 0) \cup (s_1, L) \in \partial\Omega_h
 \end{aligned}
 \tag{3}$$

where $\Omega \subset \mathbb{R}^2$ is a square domain with length = 1 unit (discretized on a Cartesian grid of size 28×28), and $\kappa(\mathbf{s})$ denotes thermal conductivity, which is assumed to be a constant and equal to 0.01 units. The goal is given a noisy measurement of temperature field u , infer the posterior QoIs of source field b . The nodal values of the temperature field are stored in the vector \mathbf{y} and those of the source field are stored in the vector \mathbf{x} .

For this numerical experiment we consider the MNIST dataset used for thermal conductivity inversion experiment. However, instead of interpreting each nodal value as conductivity, we will now treat it as source term, (so our source field will vary between 1 to 10 units).

Figure 4 shows result for this problem for test set samples. The left panel of Figure 4 shows temperature field - both with (additive Gaussian noise with variance = 1) and without noise. The obtained results for the noisy temperature measurement field are shown in the right panel. Specifically, we show MAP, mean, and standard deviation estimates and compare it against optimal reconstruction result obtained via TV regularization method. As can be observed, TV fails to capture overall contrast and boundaries of the source field, whereas MAP and mean-based reconstruction from GAN-priors are significantly better and closer to true field. The standard deviation value is elevated in the interface regions of high and low source field. This is consistent with what is to be expected for such experiment.

4 Details of WGAN-GP architecture, MCMC sampling, and training hyperparameters

In this section we provide details about different modeling choices and hyper-parameters used in this study. In all numerical experiments we use WGAN-GP [7] for learning the prior density. The detailed architecture and associated hyper-parameters used in training of this model for different numerical experiments is provided in Table 2 and Figures 5 and 6. Once the prior density is learned, posterior sampling is performed using Hamiltonian Monte Carlo method. The associated hyper-parameter values for this step is also provided in Table 2.

Some notes regarding nomenclature used in these figures:

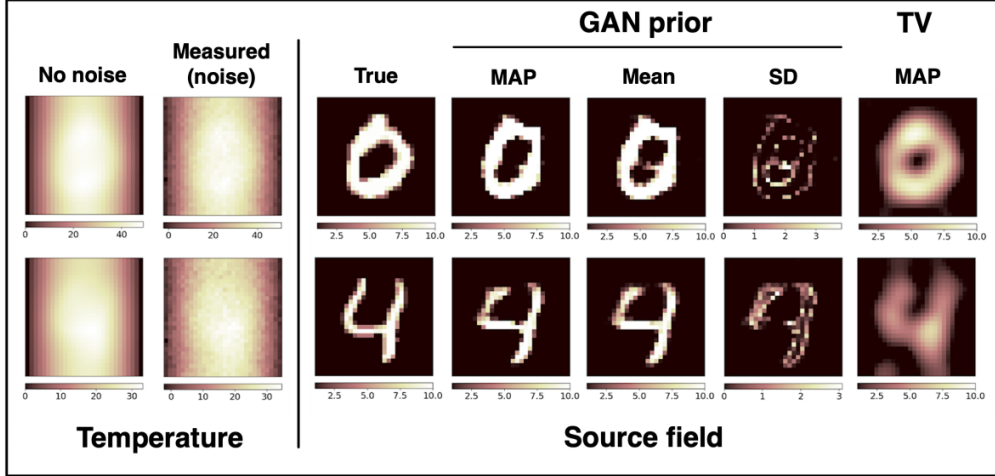


Figure 4: Source identification from noisy temperature measurement (MNIST dataset).

- Conv ($H \times W \times C \mid s=n$): convolutional layer with filter size of $H \times W$ and number of filters = C with stride (s)= n .
- TrConv ($H \times W \times C \mid s=n$): transposed convolutional layer with filter size of $H \times W$ and number of filters = C with stride (s)= n .
- FC (x, y): fully connected layer with x neurons in input and y neurons in output.
- BN : Batch Norm, LN : Layer Norm, BI ($\times 2$) : Bi-linear Interpolation (upsampling by a factor of 2).
- LReLU = Leaky ReLU with $\alpha=0.2$.

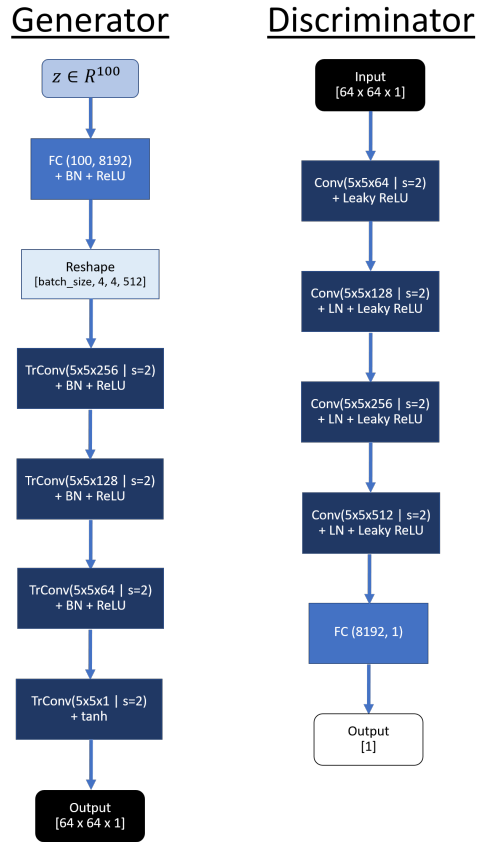
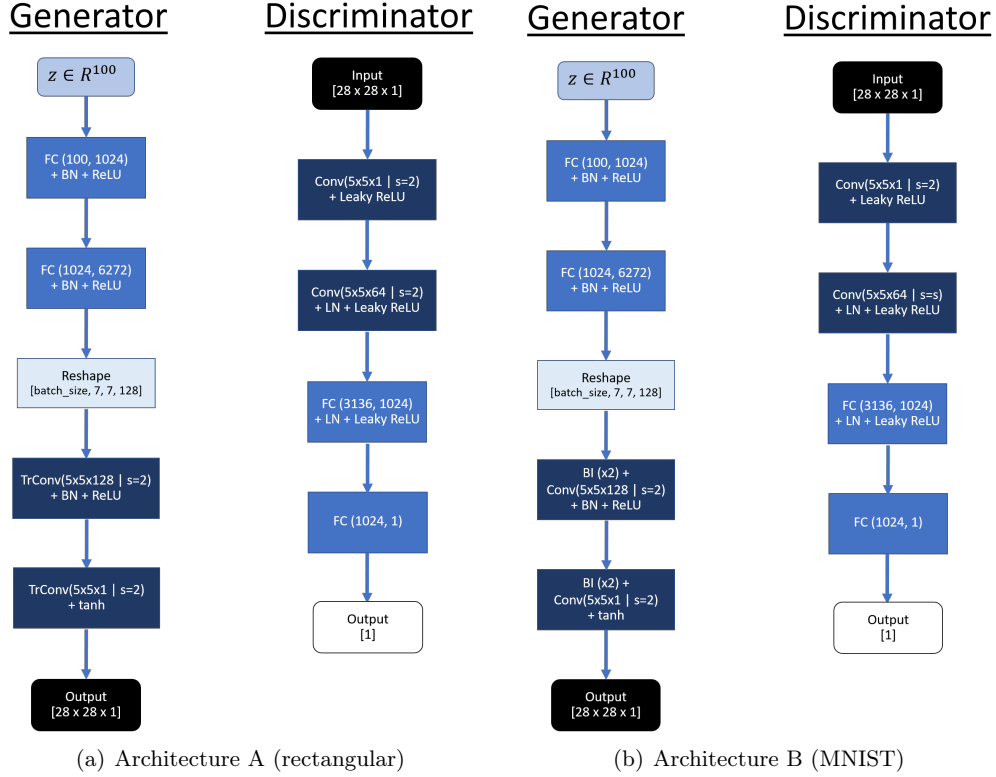
References

- [1] N. Petra, H. Zhu, G. Stadler, T. J. Hughes, and O. Ghattas, “An inexact Gauss-Newton method for inversion of basal sliding and rheology parameters in a nonlinear Stokes ice sheet model,” *Journal of Glaciology*, vol. 58, pp. 889–903, sep 2012.
- [2] D. Calvetti, S. Morigi, L. Reichel, and F. Sgallari, “Tikhonov regularization and the L-curve for large discrete ill-posed problems,” *Journal of Computational and Applied Mathematics*, vol. 123, pp. 423–446, nov 2000.
- [3] J. R. Cannon and S. P. Esteva, “An inverse problem for the heat equation,” *Inverse Problems*, vol. 2, pp. 395–403, nov 1986.
- [4] J. R. Cannon and P. Duchateau, “Structural identification of an unknown source term in a heat equation,” *Inverse Problems*, vol. 14, pp. 535–551, jun 1998.
- [5] J. Su and A. J. Silva Neto, “Two-dimensional inverse heat conduction problem of source strength estimation in cylindrical rods,” *Applied Mathematical Modelling*, vol. 25, pp. 861–872, oct 2001.

Table 2: Hyper-parameters for WGAN-GP model

Inverse problem		Inverse Heat Conduction			Inverse Radon transform	Elastography
Dataset		Rectangular	MNIST	Cahn-Hilliard microstructure	Shepp-Logan phantom	Circular phantom
Learning prior	Architecture	Type A	Type B	Type C	Type D	Type E
	Epochs	100	1000	500	500	500
	Learning rate	0.0002	0.0002	0.0001	0.0002	0.0002
	Batch size	64	64	64	100	64
	n_{critic}/n_{gen}	2	5	5	4	5
	Optimizer	Adam	Adam	Adam	RMSProp	RMSProp
Posterior sampling	Optimizer params. (β_1, β_2 or decay)	0.5, 0.999	0.5, 0.999	0.5, 0.999	0.9	0.9
	No. of MCMC samples	15k	15k	25k	64K	15k
	Burn-in period	0.5	0.5	0.5	0.5	0.5

- [6] W. Cheng, L. L. Zhao, and C. L. Fu, “Source term identification for an axisymmetric inverse heat conduction problem,” *Computers and Mathematics with Applications*, vol. 59, pp. 142–148, jan 2010.
- [7] I. Gulrajani, F. Ahmed, M. Arjovsky, V. Dumoulin, and A. C. Courville, “Improved training of wasserstein gans,” in *Advances in neural information processing systems*, pp. 5767–5777, 2017.



(c) Architecture C (two-phase microstructure)

Figure 5: Generator and discriminator architectures (type A, B, and C) of WGAN-GP for inverse heat conduction experiment.

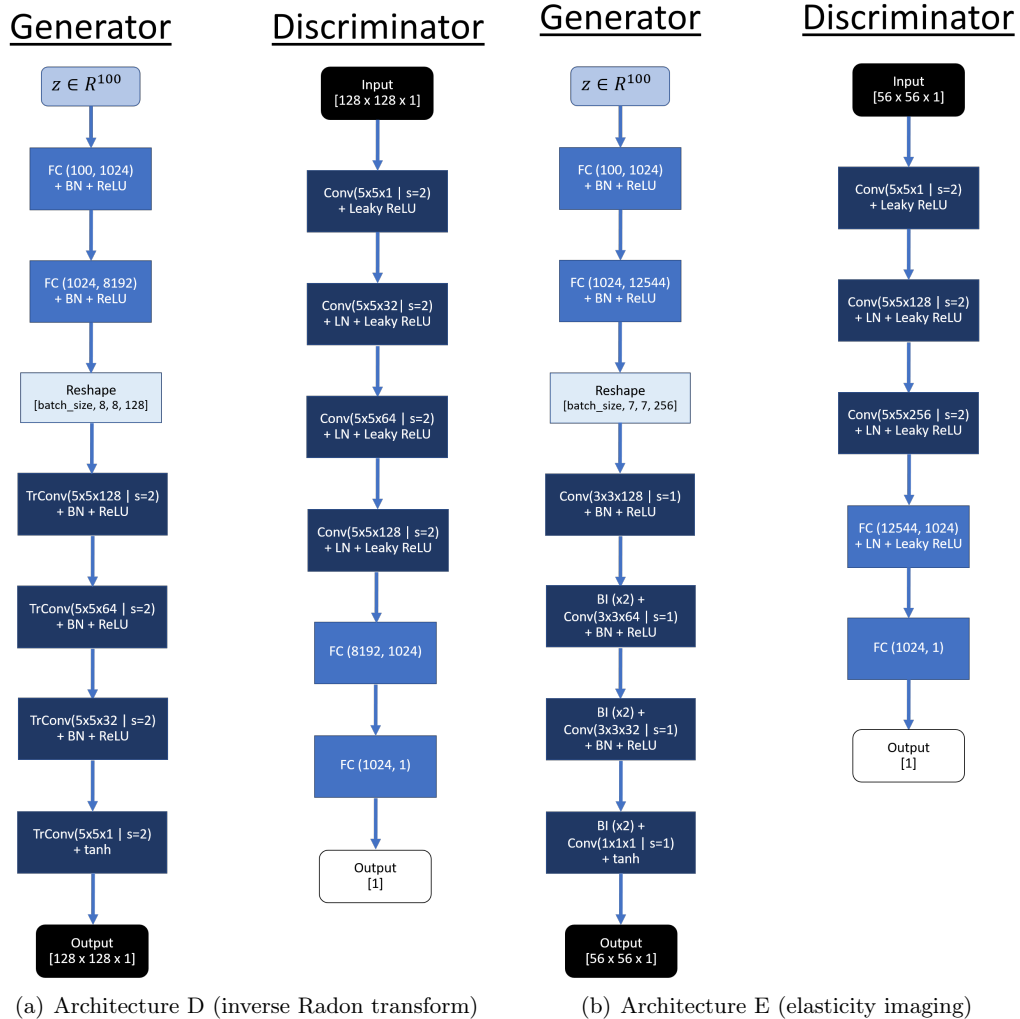


Figure 6: Generator and discriminator architectures of WGAN-GP for inverse Radon transform and elasticity imaging experiment respectively.